Preparation of Ag$_3$PO$_4$/TiO$_2$(B) Heterojunction Nanobelt with Extended Light Response and Enhanced Photocatalytic Performance

Yong Li [1,2,3,†], Yanfang Liu [1,2,†], Mingqing Zhang [1,2], Qianyu Zhou [1,2], Xin Li [1,2], Tianlu Chen [3,*] and Shifeng Wang [1,2,3,*]

1   Department of Physics, and Innovation Center of Materials for Energy and Environment Technologies, College of Science, Tibet University, Lhasa 850000, China; xzuliyong@utibet.edu.cn (Y.L.); liuyanfang@utibet.edu.cn (Y.L.); mingqing@utibet.edu.cn (M.Z.); Zhouqianyu@utibet.edu.cn (Q.Z.); lixin@utibet.edu.cn (X.L.)
2   Institute of Oxygen Supply, Center of Tibetan Studies (Everest Research Institute), Tibet University, Lhasa 850000, China
3   Key Laboratory of Cosmic Rays (Tibet University), Ministry of Education, Lhasa 850000, China
*   Correspondence: chentl@ihep.ac.cn (T.C.); wsf@utibet.edu.cn (S.W.); Tel.: +86-891-6693989 (T.C. & S.W.)
†   Both authors contributed equally to this manuscript.

Abstract: Photocatalytic degradation, as an emerging method to control environmental pollution, is considered one of the most promising environmental purification technologies. As Tibet is a region with some of the strongest solar radiation in China and even in the world, it is extremely rich in solar energy resources, which is ideal for applying photocatalytic technology to its ecological environment protection and governance. In this study, Na$_2$Ti$_3$O$_7$ nanobelts were prepared via a hydrothermal method and converted to TiO$_2$·xH$_2$O ion exchange, which was followed by high-temperature calcination to prepare TiO$_2$(B) nanobelts ("B" in TiO$_2$(B) means "Bronze phase"). A simple in situ method was used to generate Ag$_3$PO$_4$ particles on the surface of the TiO$_2$ nanobelts to construct a Ag$_3$PO$_4$/TiO$_2$(B) heterojunction composite photocatalyst. By generating Ag$_3$PO$_4$ nanoparticles on the surface of the TiO$_2$(B) nanobelts to construct heterojunctions, the light absorption range of the photocatalyst was successfully extended from UV (ultraviolet) to the visible region. Furthermore, the recombination of photogenerated electron–hole pairs in the catalyst was inhibited by the construction of the heterojunctions, thus greatly enhancing its light quantum efficiency. Therefore, the prepared Ag$_3$PO$_4$/TiO$_2$(B) heterojunction composite photocatalyst greatly outperformed the TiO$_2$(B) nanobelt in terms of photocatalytic degradation.

Keywords: photocatalyst; heterojunction; photocatalytic degradation; TiO$_2$(B) nanobelts

1. Introduction

The Qinghai–Tibet Plateau is the ecological security barrier of China and the origin of many rivers in China and South Asia. Therefore, it is of great significance to protect and manage its ecological environment [1–3]. As an emerging environmental pollution control technology, photocatalytic degradation is considered one of the most promising environmental purification technologies at present because of its advantages of mild reaction conditions, low secondary pollution, sustainability, and environmental friendliness [4–7]. Since Tibet is one of the regions with the strongest solar radiation in China and even the world, the abundant energy resource is ideal for applying photocatalytic technology to ecological environment protection and governance in Tibet [8–10]. TiO$_2$ is recognized as one of the best photocatalyst materials with stable properties, low cost, ease of access, non-toxicity and safety, and good resistance to photocorrosion. However, TiO$_2$ has a band gap as large as 3.2 eV and hence is photocatalytically active only under UV light, which

accounts for merely approximately 5% of solar radiation energy. Therefore, TiO_2 as a photocatalyst has a low utilization of solar radiation energy and insignificant photocatalytic performance [11–13]. However, combining TiO_2 with other narrow-band-gap semiconductor materials to construct heterojunctions can effectively enhance the photocatalytic performance of TiO_2. This is because, first, the introduction of narrow-band-gap semiconductors can extend the light-absorption range of TiO_2 from the UV region to the visible region, greatly increasing the material's absorption range of the solar spectrum; second, the construction of heterojunctions can effectively promote the separation of photogenerated electrons and holes, thereby improving the quantum yield of photogenerated carriers participating in photocatalytic redox reactions [13–15]. Current studies show that the use of Ag_3PO_4 compounded with TiO_2 can effectively enhance TiO_2 photocatalytic performance, but most studies use common anatase phase TiO_2 [16–19], and monoclinic (space group C2/m) TiO_2(B) has rarely been studied, while TiO_2(B) has better electrical conductivity, a sparse porous structure, and stronger photogenerated hole oxidation, and these properties make it possible for TiO_2(B) to obtain stronger photocatalytic performance by compounding [20–23]. In this study, $Na_2Ti_3O_7$ nanobelts were successfully prepared via hydrothermal methods and further used as a precursor for ion exchange with H^+ in 0.1 M dilute HCl to obtain TiO_2 hydrate, which was dried and calcined to obtain TiO_2(B) nanobelts. Throughout the preparation process, the morphology of the $Na_2Ti_3O_7$ nanobelts was maintained. $Na_2Ti_3O_7$ had good adsorption properties, as did TiO_2(B) with the same morphology, which was beneficial to its absorption of sunlight and photocatalytic degradation performance. Finally, Ag_3PO_4 nanoparticles were generated on the surface of the TiO_2(B) nanobelts via a simple in situ method, thereby successfully constructing Ag_3PO_4/TiO_2(B) heterojunctions, which substantially enhanced the photocatalytic degradation performance of TiO_2(B).

2. Results and Discussion

Figure 1a,b present SEM (Scanning Electron Microscope) images of $Na_2Ti_3O_7$ and the TiO_2(B) nanobelt, respectively, which show that they had the same morphology and were both belt-like. Therefore, TiO_2(B) prepared from $Na_2Ti_3O_7$ using the experimental method in this study was able to well-maintain the morphology of $Na_2Ti_3O_7$. Figure 1c shows EDS (Energy-Dispersive X-Ray Spectroscopy Spectra) of $Na_2Ti_3O_7$; Na, O, and Ti appear in the spectra, which verifies the chemical composition of the prepared product. Figure 1d shows EDS spectra of TiO_2(B); O and Ti appear in the spectra, which verifies the chemical composition of the prepared product. Figure 1e shows XRD (X-Ray Diffraction) patterns of TiO_2, the analysis of which revealed that the TiO_2(B) nanobelts prepared in this experiment did not belong to the rutile, anatase, or brookite phases common to TiO_2 in nature, but they did belong to a monoclinic crystal system (space group C2/m).

Figure 2a shows TEM (Transmission Electron Microscopy) diffraction patterns of the TiO_2(B) nanobelts, and Figure 2b shows the diffraction spots of crystal planes (0 2 0), $(0\ \bar{2}\ 0)$, $(6\ 0\ \bar{3})$, and $(\bar{6}\ 0\ 3)$ as calculated using the crystal structure data measured via XRD. Comparing the two images revealed that the measured and theoretically calculated results were in good agreement. In addition, the regular lattice pattern of the diffraction spots also indicated a high crystallinity of the prepared TiO_2 nanobelts. This is also confirmed by Figure 2d, which clearly shows a uniform distribution of TiO_2 grains. Figure 2c shows that the (0 2 0) crystal planes were uniformly arranged with a measured crystal plane spacing of 0.188 nm, which agreed very well with that measured via XRD. The above TEM test analysis further confirmed that the crystal structure of the TiO_2(B) nanobelts did not belong to the rutile, anatase, or brookite phases of TiO_2 that are common in nature but was a new phase of TiO_2 that is not commonly found in nature.
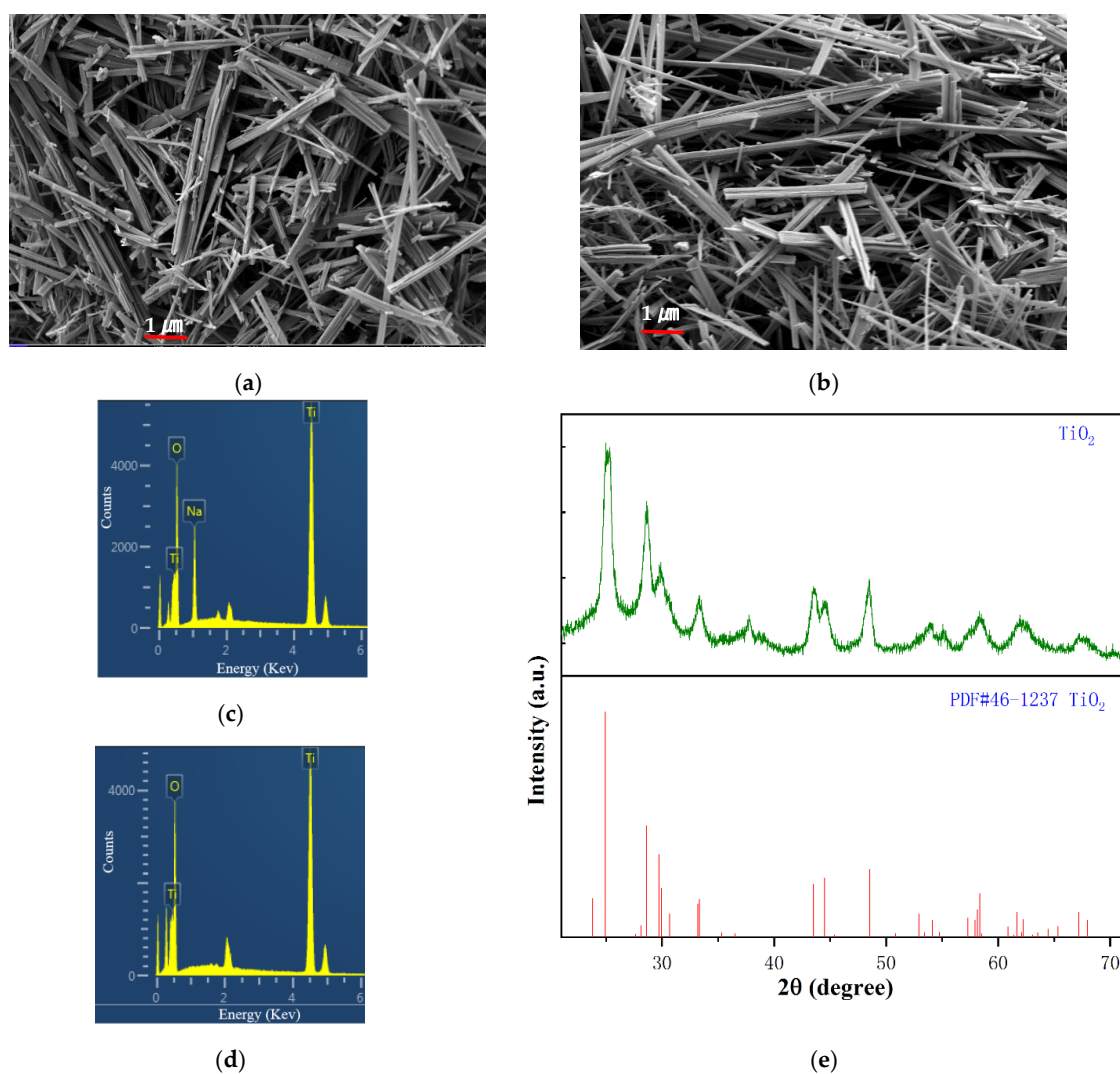
Figure 1. (**a**) SEM image of Na$_2$TiO$_7$ nanobelt; (**b**) SEM image of TiO$_2$ nanobelt; (**c**,**d**) EDS spectra of TiO$_2$ and Na$_2$Ti$_3$O$_7$ nanobelt; (**e**) XRD patterns of TiO$_2$. EDS, energy-dispersive X-ray spectroscopy.
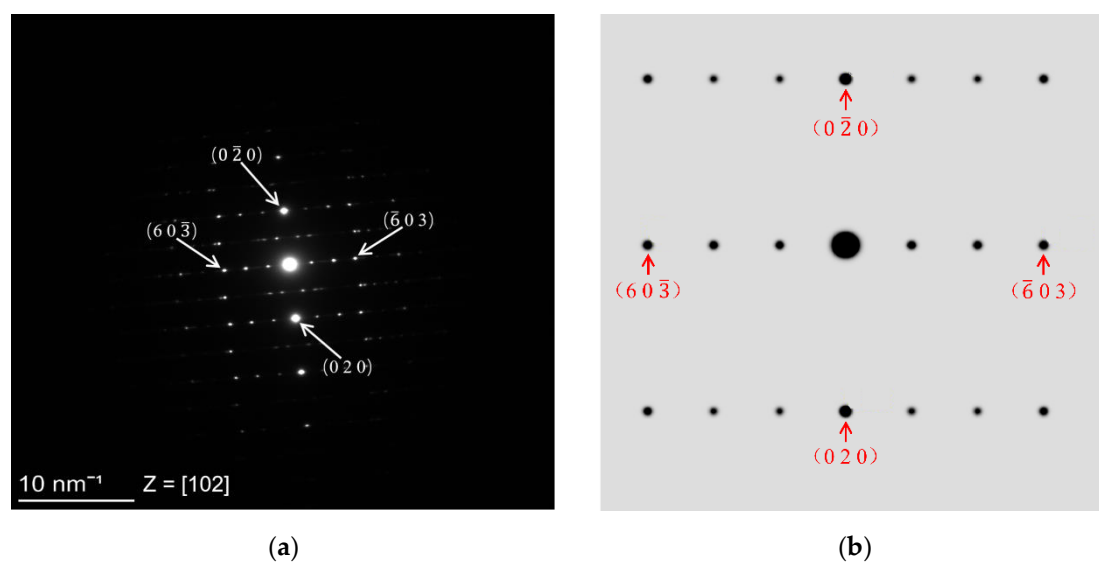

Figure 2. *Cont.*
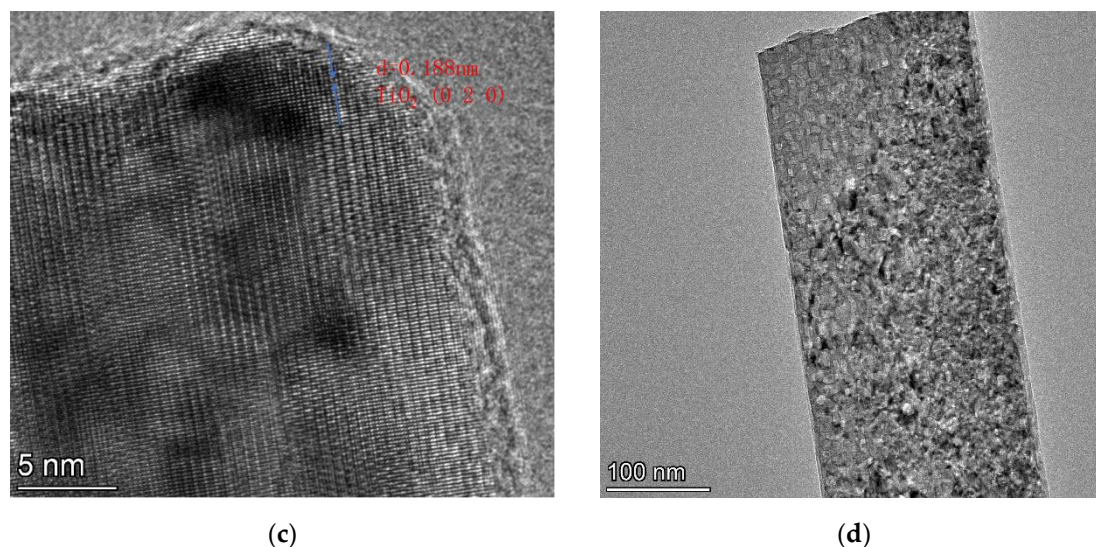
(**c**)

(**d**)

Figure 2. (**a**,**b**) Diffraction patterns of TiO$_2$(B) nanobelt; (**c**,**d**) HRTEM (High-Resolution Transmission Electron Microscopy) images of TiO$_2$(B) nanobelt.

Figure 3 shows XRD patterns of the samples. The phases of the TiO$_2$(B) nanobelts and prepared Ag$_3$PO$_4$ are analyzed in the left panel of Figure 3, with the standard powder diffraction file (PDF) cards PDF#06-0505 and PDF#46-1237, corresponding to Ag$_3$PO$_4$ and TiO$_2$(B), respectively. It can be clearly seen from the diffraction patterns that the crystallinity of Ag$_3$PO$_4$ was significantly better than that of the TiO$_2$(B) nanobelts, and the diffraction peaks of Ag$_3$PO$_4$ corresponded very well to the standard PDF card. The right panel of Figure 3 shows XRD diffraction patterns of the composites of Ag$_3$PO$_4$ and TiO$_2$(B) with different molar ratios. There were very obvious diffraction peaks of Ag$_3$PO$_4$ in the composites, and the relative intensity of the peaks did not change significantly with the increase in the molar ratio of Ag$_3$PO$_4$. Among the diffraction peaks of TiO$_2$(B), only the strongest diffraction peak, corresponding to the (110) plane, was weakly reflected in the composite, and it weakened with the increase in the molar ratio of Ag$_3$PO$_4$.
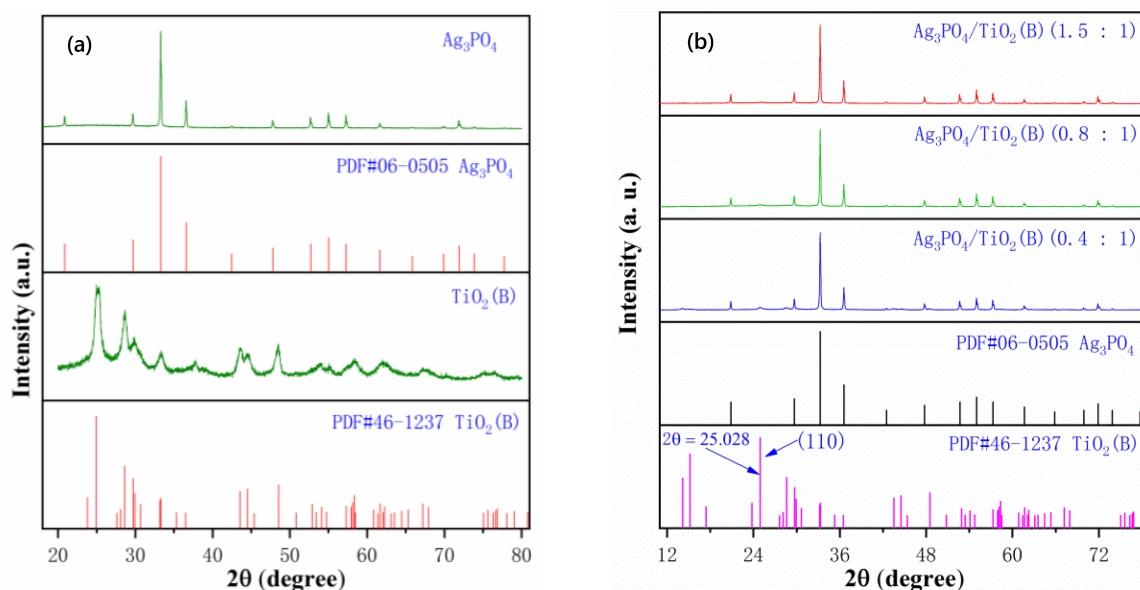

Figure 3. (**a**) XRD patterns of Ag$_3$PO$_4$ and TiO$_2$(B); (**b**) XRD patterns of Ag$_3$PO$_4$/TiO$_2$(B) with different molar ratios.

Figure 4 shows SEM and mapping images of the $Ag_3PO_4/TiO_2(B)$ composite, where Figure 4a shows a SEM image when the molar ratio of Ag_3PO_4 to TiO_2 was 0.4:1, and Figure 4b shows the SEM image when the molar ratio increased to 1.5:1. The Ag_3PO_4 particles were clearly attached to the surface of belt-like $TiO_2(B)$, and the number of Ag_3PO_4 particles increased as the molar ratio of Ag_3PO_4 increased. EDS mapping (Figure 4c–f) showed that the sample contained Ti, O, Ag, and P elements, which were uniformly distributed in the area where the composite was located, indicating that the composite contained Ag_3PO_4 and $TiO_2(B)$, and the two were distributed relatively uniformly.
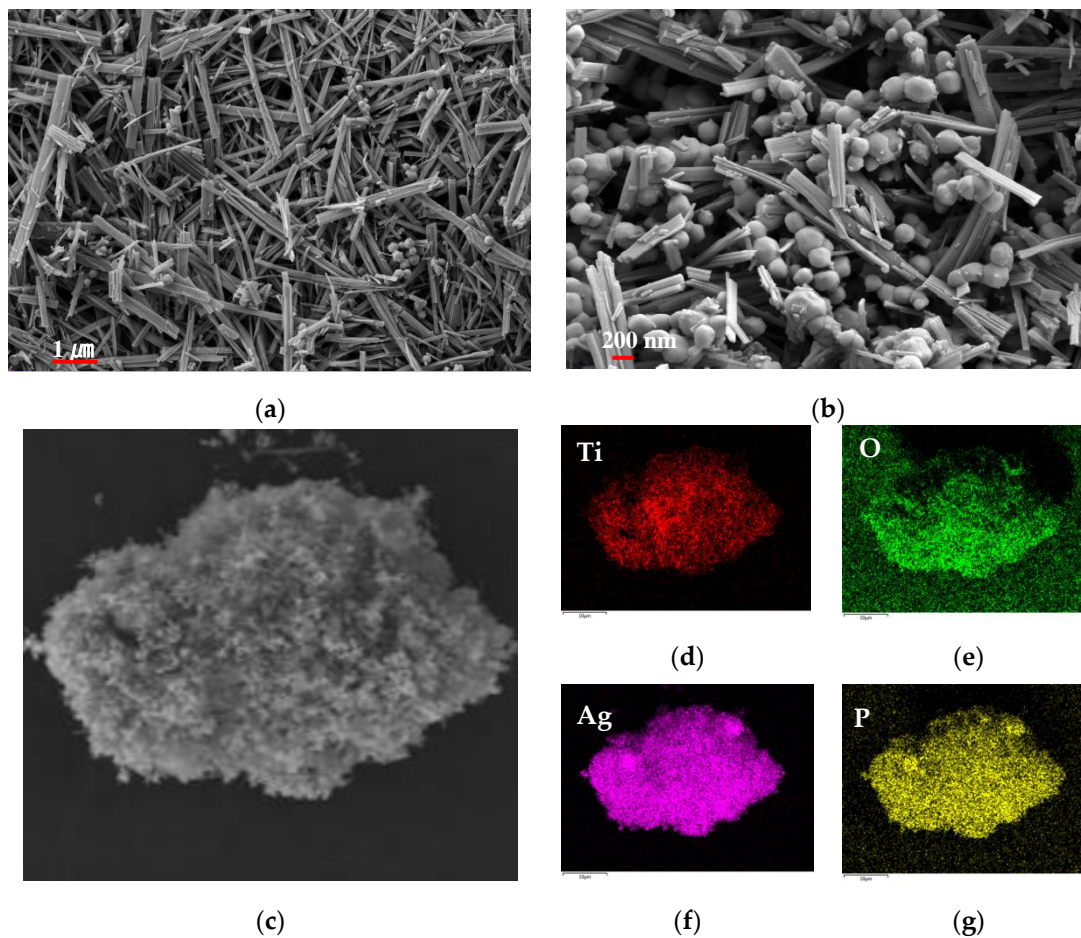

(**a**) (**b**)

(**c**) (**d**) (**e**) (**f**) (**g**)

Figure 4. (**a**,**b**) SEM images of Ag_3PO_4/TiO_2 composite; (**c**) The SEM image corresponding to map; (**d**) Map of Ti; (**e**) Map of O; (**f**) Map of Ag; (**g**) Map of P.

The left panel of Figure 5 shows the photocatalytic degradation curves of RhB solution by $Ag_3PO_4/TiO_2(B)$ composites with different molar ratios. It can be seen that the $TiO_2(B)$ nanobelts degraded RhB slowly, and the degradation rate was less than 20% after 30 min of degradation. After combining with Ag_3PO_4, the photocatalytic degradation of RhB by the composite product was improved, particularly when increasing the molar ratio of Ag_3PO_4. When the molar ratio of Ag_3PO_4 to $TiO_2(B)$ increased to 1.5:1, within 30 min, the composite photocatalyst achieved nearly 100% degradation of RhB, and the photocatalytic performance increased by nearly five times, which was much higher than the photocatalytic degradation performance of commercial P_{25}. The right panel of Figure 5 shows actual photographs of the color change of RhB solution due to photocatalytic degradation by $Ag_3PO_4/TiO_2(B)$ composites with different molar ratios. These photographs visually demonstrate the rapid enhancement of the photocatalytic performance of the composite with the increase in the molar ratio of Ag_3PO_4. The $Ag_3PO_4/TiO_2(B)$ composite was obtained on the surface of the $TiO_2(B)$ nanobelts through the in situ growth of Ag_3PO_4

crystal grains. Compared with that of the TiO_2(B) nanobelts, the photocatalytic performance of the composite increased rapidly with the increase in the molar ratio of Ag_3PO_4. When the molar ratio of Ag_3PO_4 to TiO_2(B) reached 1.5:1, the photocatalytic performance of the composite far exceeded (was nearly five times) that of the pure TiO_2(B) nanobelt. We believe that the enhancement of the photocatalytic ability of the composite was, first, due to the introduction of Ag_3PO_4, which greatly expanded the absorption range of the material within the solar spectrum and enhanced the absorption of visible light [24–26] and, second, because of the construction of heterojunctions, which promoted the separation of photogenerated electron–hole pairs and inhibited their recombination [27–29]. In addition, it can be seen from the mapping results that the two substances constructed heterojunctions that were highly uniformly distributed, which gave full play to their role in the composite.
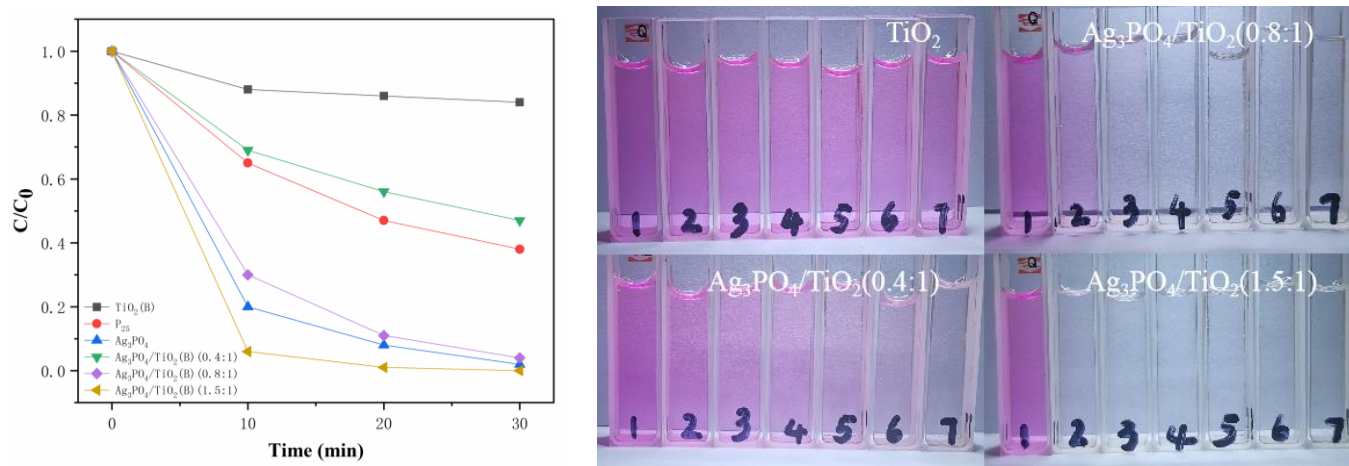

Figure 5. Photocatalytic degradation curves and images of Ag_3PO_4/TiO_2 composite.

Figure 6 shows the absorbance curves of the samples against a continuous spectrum. This test investigated the variation curves of absorbance of the TiO_2(B) nanobelts and Ag_3PO_4 in the visible region (wavelength > 400 nm). It was obvious that the light-absorption ability of Ag_3PO_4 was significantly higher than that of the TiO_2(B) nanobelts in the visible region. After the TiO_2(B) nanobelts and Ag_3PO_4 formed a composite, its visible-light-absorption ability was enhanced to some extent compared with that of the TiO_2(B) nanobelts, indicating that the introduction of Ag_3PO_4 enhanced the visible light absorption ability of the composite.
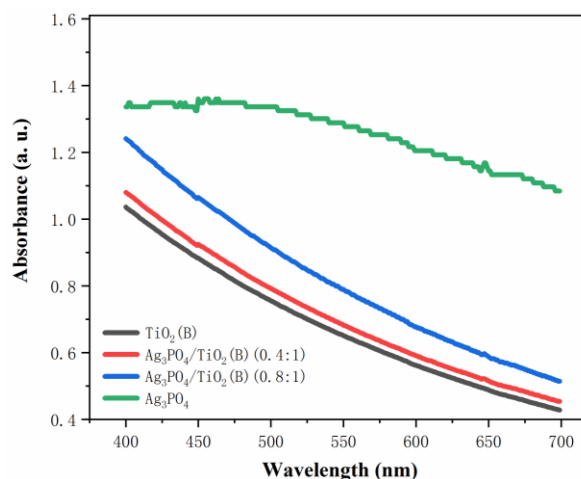

Figure 6. Continuous spectra of absorbance of synthesized samples.

To investigate the recombination and migration of photogenerated electrons before and after the combination of Ag_3PO_4 and $TiO_2(B)$, we tested their PL (photoluminescence) spectra and photocurrent curves, respectively, as shown in Figure 7. As can be clearly seen from the PL spectrum in the left panel of Figure 7, the peaks of the PL lines of the $TiO_2(B)$ nanobelts were the strongest, while the peaks of the PL lines of the composite decreased rapidly with the increase in the molar ratio of the added Ag_3PO_4. Stronger fluorescence reflects an easier recombination of the photogenerated electron–hole pairs of the substance, making it difficult for the photogenerated electron–hole pairs to migrate to the surface of the catalyst to participate in the photocatalytic redox reaction, which is not conducive to the performance of photocatalysis [30–32]. The right panel of Figure 7 shows the photocurrent curves of the samples. The photocurrents of pure $TiO_2(B)$ nanobelts and Ag_3PO_4 nanoparticles were the lowest. In comparison, the photocurrent of $Ag_3PO_4/TiO_2(B)$ composite was enhanced and increased continuously with the increase in the molar ratio of Ag_3PO_4, reaching a maximum when the molar ratio of Ag_3PO_4 was increased to 1.5:1. These two sets of curves well explained the underlying reason for the variation pattern of photocatalytic performance in Figure 5 and also indirectly proved that Ag_3PO_4 nanoparticles grown on the surface of $TiO_2(B)$ nanobelts through our simple in situ method indeed successfully constructed a $Ag_3PO_4/TiO_2(B)$ heterojunction composite, effectively promoting the separation of photogenerated charges and thereby enhancing the photocatalytic performance of the composite catalyst.
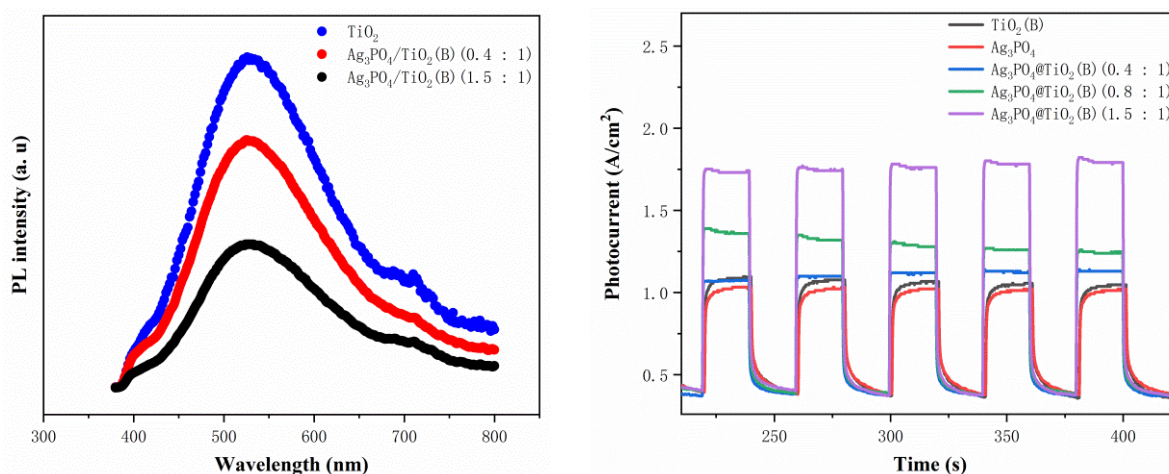

Figure 7. PL and photocurrent spectra of synthesized samples.

3. Materials and Experiment

3.1. Materials

Regarding the chemicals used in the experiment, NaOH and nano-TiO_2 were purchased from Aladdin Industries, Inc.(Shanghai, China), $Na_2HPO_4 \cdot 12H_2O$ from Chengdu Jinshan Chemical Reagent Co., Ltd. (Chengdu, China), $AgNO_3$ from Sinopharm Chemical Reagent Co., Ltd. (Shanghai, China), and Rhodamine B (RhB, $C_{28}H_{31}ClN_2O_3$) from Beijing Solarbio Technology Co., Ltd. (Beijing, China). All the reagents were analytically pure and used without further purification.

3.2. Preparation of $TiO_2(B)$ Nanobelt, Ag_3PO_4, and $Ag_3PO_4/TiO_2(B)$

Nano-TiO_2 (1 g) was added to 100 mL of 10 M NaOH aqueous solution, stirred evenly, poured into a 150 mL hydrothermal reactor, heated to 200 °C, and held for 24 h before cooling naturally. Then, the reaction product was taken out of the reactor and rinsed with a large amount of deionized (DI) water to a nearly neutral pH, which was followed by vacuum filtration and drying to obtain the $Na_2Ti_3O_7$ nanobelts. After that, $Na_2Ti_3O_7$ was soaked in 0.1 M dilute HCl for 72 h to allow ion exchange between H^+ and Na^+ in $Na_2Ti_3O_7$ to obtain $TiO_2 \cdot xH_2O$, which was rinsed with a large amount of DI water until the pH of the

solution was nearly neutral, vacuum filtered, dried at 60 °C in a blast drying oven, calcined at 500 °C in a muffle furnace with a heating rate of 1 °C/min for 2 h, and cooled naturally to obtain the $TiO_2(B)$ nanobelts. To prepare $Ag_3PO_4/TiO_2(B)$, 100 mg of the prepared $TiO_2(B)$ nanobelts was weighed first, and corresponding masses of Ag_3PO_4 were calculated according to molar ratios of (1:0.4), (1:0.8), and (1:1.5), respectively, as were the corresponding masses of $AgNO_3$ and $Na_2HPO_4 \cdot 12H_2O$ required for the preparation of Ag_3PO_4. Then, 100 mg of the TiO_2 nanobelts and the corresponding mass of $Na_2HPO_4 \cdot 12H_2O$ were added into 100 mL of DI water, which was followed by ultrasonication for 30 min. Next, the corresponding mass of $AgNO_3$ was dissolved in 50 mL of DI water and then slowly added into the sonicated mixture with constant stirring. Finally, the mixture was vacuum-filtrated and dried to obtain composites with different molar ratios, which were labeled as $Ag_3PO_4/TiO_2(B)$ (0.4:1), $Ag_3PO_4/TiO_2(B)$ (0.8:1), and $Ag_3PO_4/TiO_2(B)$ (1.5:1). Ag_3PO_4 was directly obtained by mixing a certain proportion of $AgNO_3$ and $Na_2HPO_4 \cdot 12H_2O$ solution, which was followed by vacuum filtration and drying.

3.3. Analysis and Testing

Field emission scanning electron microscopy (FE-SEM, Gemini SEM 300, Manufactured by Zeiss, Oberkochen, Germany) and field emission transmission electron microscopy (FE-TEM, FEI Talos F200X, Manufactured by FEI, Hillsboro, OR, USA) were used to observe and analyze the morphology of the samples as well as test and analyze the elemental composition and distribution of the samples. FE-TEM (FEI Talos F200X, Manufactured by FEI, USA) and X-ray powder diffractometry (XRD, Bruker D8 Advance, Manufactured by Bruker, Bremen, Germany) were used to test and analyze the crystal structure and phase of the samples. A fluorescence spectrometer (PL FLS 1000/FS5, Manufactured by Edinburgh, UK) was used to test the fluorescence emission spectra of the samples. An electrochemical workstation (CHI-760E, Manufactured by Chenhua, Shanghai, China) was used to test the photocurrent of the samples. A UV-Vis spectrophotometer (UV-1200, Manufactured by Macy, Shanghai, China) was used to test and analyze changes in photocatalytic degradation performance, as well as obtain absorbance curves of the samples for RhB. In addition, a muffle furnace (KSL-1700X, Manufactured by Kejing, Hefei, China), a blast drying oven (DHG-9246A, Manufactured by Kejing, Hefei, China), and a benchtop high-speed centrifuge (LC-LX-H185C, Manufactured by Lichen, Shanghai, China) were also used to prepare the experimental materials.

3.4. Photocatalytic Performance Test

Each sample (20 mg) was added to 100 mL of 20 mg/L RhB solution and sonicated for 30 min. The mixture was placed under a light source simulated by a solar simulator (Solar-500Q, Manufactured by Newbit, Beijing, China), with the intensity of the light source adjusted to obtain a light intensity of 600 W/m^2 at the liquid surface. Approximately 6 mL of the experimental liquid was taken every 10 min and placed into the centrifuge for 10 min at 10,000 r/min. The supernatant was taken and tested by the UV-Vis spectrophotometer for absorbance A_n (n = experimental serial number, with 1 for the first sample taken). Since the absorbance is proportional to the concentration of the solution (C_n), then there is a solution concentration ratio $C_n/C_0 = A_n/A_0$ (A_0 = absorbance of the 20 mg/L of RhB solution, C_0 = concentration of the 20 mg/L of RhB solution). The absorbance of each sample was measured at 10-min intervals for 60 min according to the above method, and the corresponding degradation rates were calculated to plot the photocatalytic degradation curve.

4. Conclusions

In this study, $Na_2Ti_3O_7$ nanobelts were successfully prepared via the hydrothermal method, and then, $TiO_2 \cdot xH_2O$ was obtained via ion exchange, which was followed by calcinating $TiO_2 \cdot xH2O$ in a muffle furnace at 500 °C for 2 h to obtain $TiO_2(B)$ nanobelts. The belt-like morphology of $Na_2Ti_3O_7$ was maintained throughout the preparation process,

which made the TiO$_2$(B) have good adsorption performance and enhanced the photocatalytic performance of the TiO$_2$(B) photocatalyst. Using AgNO$_3$ and Na$_2$HPO$_4$·12H$_2$O as reactants, Ag$_3$PO$_4$ nanoparticles were generated on the surface of the TiO$_2$(B) nanobelts by a simple in situ method, thereby successfully preparing Ag$_3$PO$_4$/TiO$_2$(B) heterojunction composites. The pure TiO$_2$(B) nanobelt degraded the simulated pollutant RhB slowly, with a degradation rate lower than 20% after 30 min of degradation. By combining the TiO$_2$(B) nanobelts with Ag$_3$PO$_4$, the performance of the composite photocatalyst was rapidly improved with the increase in the molar ratio of Ag$_3$PO$_4$, and the composite was able to degrade nearly 100% of RhB in 30 min when the molar ratio of Ag$_3$PO$_4$ to TiO$_2$ was increased to 1.5:1. The improvement of the photocatalytic performance of the Ag$_3$PO$_4$/TiO$_2$(B) composite was mainly attributed to the successful construction of heterojunctions between Ag$_3$PO$_4$ and TiO$_2$(B), thereby greatly inhibiting the recombination of photogenerated electron–hole pairs and enhancing the light quantum yield of the photocatalyst. In addition, the introduction of Ag$_3$PO$_4$ in the composite successfully extended the light absorption range of the photocatalyst into the visible region, thus improving the utilization of simulated sunlight. Based on the above two reasons, the photocatalytic performance of the Ag$_3$PO$_4$/TiO$_2$(B) composite was significantly improved.

Institutional Review Board Statement: Not applicable.

Informed Consent Statement: Not applicable.

Data Availability Statement: Not applicable.

Conflicts of Interest: The authors declare no conflict of interest.

Sample Availability: Samples are available from Yong Li on valid request.

References

1. Liu, J.; Milne, R.I.; Cadotte, M.W.; Wu, Z.-Y.; Provan, J.; Zhu, G.-F.; Gao, L.-M.; Li, D.-Z. Protect Third Pole's fragile ecosystem. *Science* **2018**, *362*, 1368. [CrossRef]
2. Yuan, Q.; Yuan, Q.; Ren, P. Coupled effect of climate change and human activities on the restoration/degradation of the Qinghai-Tibet Plateau grassland. *J. Geogr. Sci.* **2021**, *31*, 1299–1327. [CrossRef]
3. Liu, S.; Wang, P.; Wang, C.; Wang, X.; Chen, J. Anthropogenic disturbances on antibiotic resistome along the Yarlung Tsangpo River on the Tibetan Plateau: Ecological dissemination mechanisms of antibiotic resistance genes to bacterial pathogens. *Water Res.* **2021**, *202*, 117447. [CrossRef]
4. Kumar, A.; Kumar, A.; Krishnan, V. Perovskite oxide based materials for energy and environment-oriented photocatalysis. *ACS Catal.* **2020**, *10*, 10253–10315. [CrossRef]
5. Li, S.-Q.; Lv, S.-Y.; Zhou, H.-Y.; Ding, Y.-Q.; Liu, Q.-Y.; Ma, J.-B. Oxidation of isoprene by titanium oxide cluster cations in the gas phase. *Phys. Chem. Chem. Phys.* **2020**, *22*, 27357–27363. [CrossRef] [PubMed]
6. Liras, M.; Barawi, M.; de la Peña O'Shea, V.A. Hybrid materials based on conjugated polymers and inorganic semiconductors as photocatalysts: From environmental to energy applications. *Chem. Soc. Rev.* **2019**, *48*, 5454–5487. [CrossRef]
7. Xie, X.; Zhang, N. Positioning MXenes in the photocatalysis landscape: Competitiveness, challenges, and future perspectives. *Adv. Funct. Mater.* **2020**, *30*, 2002528. [CrossRef]

8. Gelsor, N.; Jin, Y.-M.; Tsoja, W.-M.; Zhou, Y.; Balma, S.; Tunzhu, D. Ground-based measurements of global solar radiation and UV radition in Tibet. *Spectrosc. Spect. Anal.* **2019**, *39*, 1683–1688.

9. Pu, Z. Suggestions on efficient development and utilization of solar energy resources in Tibet. *IOP Conf. Ser. Earth Environ. Sci.* **2021**, *804*, 032030. [CrossRef]

10. Liu, D.; Yang, M.; Shi, Z.; Ning, L. Research on consumptive capacity and countermeasures of renewable energy of central Tibet. *J. Renew. Sustain. Energy* **2017**, *9*, 025902. [CrossRef]

11. Fu, C.; Li, F.; Zhang, J.; Li, D.; Qian, K.; Liu, Y.; Tang, J.; Fan, F.; Zhang, Q.; Gong, X.Q.; et al. Site sensitivity of interfacial charge transfer and photocatalytic efficiency in photocatalysis: Methanol oxidation on anatase TiO_2 nanocrystals. *Angew. Chem.* **2021**, *133*, 6225–6234. [CrossRef]

12. Song, Y.; Ling, L.; Westerhoff, P.; Shang, C. Evanescent waves modulate energy efficiency of photocatalysis within TiO_2 coated optical fibers illuminated using LEDs. *Nat. Commun.* **2021**, *12*, 4101. [CrossRef]

13. Lu, Y.; Liu, X.-L.; He, L.; Zhang, Y.-X.; Hu, Z.-Y.; Tian, G.; Cheng, X.; Wu, S.-M.; Li, Y.-Z.; Yang, X.-H.; et al. Spatial heterojunction in nanostructured TiO_2 and its cascade effect for efficient photocatalysis. *Nano Lett.* **2020**, *20*, 3122–3129. [CrossRef] [PubMed]

14. Xu, F.; Meng, K.; Cheng, B.; Wang, S.; Xu, J.; Yu, J. Unique S-scheme heterojunctions in self-assembled $TiO_2/CsPbBr_3$ hybrids for CO_2 photoreduction. *Nat. Commun.* **2020**, *11*, 4613. [CrossRef]

15. Lan, K.; Wei, Q.; Wang, R.; Xia, Y.; Tan, S.; Wang, Y.; Elzatahry, A.; Feng, P.; Mai, L.; Zhao, D. Two-dimensional mesoporous heterostructure delivering superior pseudocapacitive sodium storage via bottom-up monomicelle assembly. *J. Am. Chem. Soc.* **2019**, *141*, 16755–16762. [CrossRef] [PubMed]

16. Liu, R.; Hu, P.; Chen, S. Photocatalytic activity of Ag_3PO_4 nanoparticle/TiO_2 nanobelt heterostructures. *Appl. Surf. Sci.* **2012**, *258*, 9805–9809. [CrossRef]

17. Saud, P.S.; Pant, B.; Twari, A.P.; Ghouri, Z.K.; Park, M.; Kim, H.Y. Effective photocatalytic efficacy of hydrothermally synthesized silver phosphate decorated titanium dioxide nanocomposite fibers. *J. Colloid Interface Sci.* **2016**, *465*, 225–232. [CrossRef]

18. Chi, C.; Pan, J.; You, M.; Dong, Z.; Zhao, W.; Song, C.; Zheng, Y.; Li, C. The porous TiO_2 nanotubes/Ag_3PO_4 heterojunction for enhancing sunlight photocatalytic activity. *J. Phys. Chem. Solids* **2018**, *114*, 173–178. [CrossRef]

19. Amaral, R.; Blois, C.; Lunz, J.; Mello, A.; Jardim, P. Physical and optical properties of Ag_3PO_4 decorated TiO_2 based nanostructures. *J. Solid State Chem.* **2022**, *305*, 122655. [CrossRef]

20. Xie, F.; Zhu, J.; Li, Y.; Shen, D.; Abate, A.; Wei, M. TiO_2-B as an electron transporting material for highly efficient perovskite solar cells. *J. Power Sources* **2019**, *415*, 8–14. [CrossRef]

21. Di, T.; Zhang, J.; Cheng, B.; Yu, J.; Xu, J. Hierarchically nanostructured porous $TiO_2(B)$ with superior photocatalytic CO_2 reduction activity. *Sci. China Chem.* **2018**, *61*, 344–350. [CrossRef]

22. Hossain, M.K.; Koirala, A.R.; Akhtar, U.S.; Song, M.K.; Yoon, K.B. First Synthesis of Highly Crystalline, Hexagonally Ordered, Uniformly Mesoporous TiO_2-B and Its Optical and Photocatalytic Properties. *Chem. Mater.* **2015**, *27*, 6550–6557. [CrossRef]

23. Chen, S.; Zhu, Y.; Li, W.; Liu, W.; Li, L.; Yang, Z.; Liu, C.; Yao, W.; Lu, X.; Feng, X. Synthesis, Features and Applications of Mesoporous Titania with $TiO_2(B)$. *Chin. J. Catal.* **2010**, *31*, 605–614. [CrossRef]

24. Silva, G.N.; Martins, T.A.; Nogueira, I.C.; Santos, R.K.; Li, M.S.; Longo, E.; Botelho, G. Synthesis of Ag_3PO_4/SnO_2 composite photocatalyst for improvements in photocatalytic activity under visible light. *Mater. Sci. Semicond. Proc.* **2021**, *135*, 106064. [CrossRef]

25. Ta, Q.T.H.; Tran, N.M.; Tri, N.N.; Sreedhar, A.; Noh, J.-S. Highly surface-active Si-doped $TiO_2/Ti_3C_2T_x$ heterostructure for gas sensing and photodegradation of toxic matters. *Chem. Eng. J.* **2021**, *425*, 131437. [CrossRef]

26. Xu, Y.; Liu, X.; Zheng, Y.; Li, C.; Yeung, K.W.K.; Cui, Z.; Liang, Y.; Li, Z.; Zhu, S.; Wu, S. Ag_3PO_4 decorated black urchin-like defective TiO_2 for rapid and long-term bacteria-killing under visible light. *Bioact. Mater.* **2020**, *6*, 1575–1587. [CrossRef] [PubMed]

27. Khalid, N.R.; Mazia, U.; Tahir, M.B.; Niaz, N.A.; Javid, M.A. Photocatalytic degradation of RhB from an aqueous solution using Ag_3PO_4/N-TiO_2 heterostructure. *J. Mol. Liq.* **2020**, *313*, 113522. [CrossRef]

28. Zhang, Y.; Duoerkun, G.; Shi, Z.; Cao, W.; Liu, T.; Liu, J.; Zhang, L.; Li, M.; Chen, Z. Construction of TiO_2/Ag_3PO_4 nanojunctions on carbon fiber cloth for photocatalytically removing various organic pollutants in static or flowing wastewater. *J. Colloid Interface Sci.* **2020**, *571*, 213–221. [CrossRef]

29. Wang, P.; Li, Y.; Liu, Z.; Chen, J.; Wu, Y.; Guo, M.; Na, P. In-situ deposition of Ag_3PO_4 on TiO_2 nanosheets dominated by (001) facets for enhanced photocatalytic activities and recyclability. *Ceram. Int.* **2017**, *43*, 11588–11595. [CrossRef]

30. Meng, Z.; Zhou, B.; Xu, J.; Li, Y.; Hu, X.; Tian, H. Heterostructured Nitrogen and Sulfur co-doped Black TiO_2/g-C_3N_4 Photocatalyst with Enhanced Photocatalytic Activity. *Chem. Res. Chin. Univ.* **2020**, *36*, 1045–1052. [CrossRef]

31. Du, J.; Xu, Z.; Li, H.; Yang, H.; Xu, S.; Wang, J.; Jia, Y.; Ma, S.; Zhan, S. Ag_3PO_4/g-C_3N_4 Z-scheme composites with enhanced visible-light-driven disinfection and organic pollutants degradation: Uncovering the mechanism. *Appl. Surf. Sci.* **2021**, *541*, 148487. [CrossRef]

32. Wu, Z.; Zhao, Y.; Mi, L.; Guo, Y.; Wang, H.; Liu, K.; Zhang, K.; Wang, B. Preparation of g-C_3N_4/TiO_2 by template method and its photocatalytic performance. *Colloids Surf. A Physicochem. Eng. Asp.* **2021**, *624*, 126756. [CrossRef]